# Multiple optical characterization of a solid/liquid material

Tanguy Davin*, Carole Gobin, Franck Lefebvre, Gilles Godard, Thibaut Ménard, Emilien Varea, Luminita Danaila

CORIA UMR 6614, University of Rouen Normandie, Avenue de l'Université, 76801 Saint-Étienne-du-Rouvray, France
*Corresponding author: davint@coria.fr

**Keywords:** 2D Flow visualization, Particle Image Velocimetry, Background Oriented Schlieren, TC scanning, Phase Change Material

ABSTRACT

Various industrial configurations use Phase Change Materials (PCM) for the thermal management. Their use generates complex flows that must be studied and characterized to better understand the phase-change mechanisms and to help model development. In particular, the works considering large containers where turbulent effects are encountered are poorly addressed in the literature.

The present study proposes the experimental analysis of PCM flows with a simultaneous flow and energetic characterization. Heat and mass transfer are analyzed in a large (0.4 meter) cubic volume undergoing various lateral temperature conditions. 2-dimensional fields of velocities by a Particle Image Velocimetry (PIV) technique and temperature by thermocouples (TC) scanning and by Background Oriented Schlieren (BOS) are measured. The measurements methodology highlights the local transfer as reflected by the Nusselt number for the two latter techniques. The local Nusselt numbers are also integrated and compared to a global Nusselt assessed by the heat transfer through the hot wall regulating system.

In this study, the different techniques with their theoretical approaches and the experimental setup are described. The conditions and the conducted procedure of the tests are detailed. The results of local measurements for two particular temperature configurations are given. The global heat transfer and the global Nusselt number are also provided as a function of the Rayleigh number and the solid fraction. The results and the techniques are discussed. The results corresponding to various Rayleigh numbers form a database that is used to understand phenomena in large PCM containers and validate numerical models involving melting phenomena.

## 1. Introduction

The so-called Phase Change Material (PCM) are interesting substances from the energy-storage viewpoint because of their high melting enthalpy. They have been studied for thermal management purposes in different application fields: buildings, automotive, electronics (Jaguemont et al., 2018; Agyenim et al., 2010; Sahoo et al., 2016; Souayfane et al., 2016; Rostami et al., 2020). The

interest in PCM increases, thus pointing to the requirement to better characterize them from a fundamental viewpoint.

The literature provides some experimental characterization of melting PCM, in particular with Particle Image Velocimetry (PIV) (Faden et al., 2019; Sun et al., 2021) in small containers. Unfortunately, most reported descriptions point to the fluid velocity, with less attention to the interface or the solid phase. Moreover, the experimental characterization is not exhaustive and considers global parameters; only few local measurements are reported (Dhaidan & Khodadadi, 2015).

The present study aims at characterizing the flow of a melting Phase Change Material and propose well-resolved measurements in a relatively wide container. The interesting physical parameters are the temperature and the velocity. As the turbulence transition is reached, their variations are also characterized. The idea is to better understand the onset of turbulence and the correlation between the fluid dynamics and the temperature field. Three different techniques are employed: Background Oriented Schlieren (BOS); Particle Image Velocimetry (PIV); thermocouples (TC) network scanning.

## 2. Experimental apparatus

The experimental bench (Figure 1) considers a thermally managed volume: a cube of 0.4-meter edge-length. Two vertical, opposite walls are temperature controlled by liquid circulation. Two other walls are made of double-glass to allow for measurements. The two last faces of the cube are thermally insulated. The flow is assumed to be two-dimensional, as sketched in the right part of Figure 1. The chamber is filled with a commercial paraffin RT28HC (Rubitherm®), seeded with rhodamine particles (Vestosint®). The particles are illuminated in the median plane by a 532 nm ND-YAG laser. A laser sheet is formed from the upper surface through a lid groove. The BOS apparatus includes a random-dots-pattern target, lighted by a white-light lamp placed behind the scene. The front-face is reserved for imaging view with two cameras triggered to obtain the BOS images between two PIV laser pulses. The scene passes through a dichroic mirror to keep the same viewpoint for both camera. The chosen cutting frequency is 550 nm to minimize the laser reflection and preserve the particles re-emission on the PIV images. Figure 2 shows the actual experimental arrangement.

Due to the relative slowness of the flow, the acquisition is performed at 4 Hz. Statistics are computed over 500 images. A six-thermocouples comb (Figure 2, right) fixed over a 2D mechanical scanner monitors the whole median plane. The 2 extremities thermocouples are more sensitive to allow measuring the temporal temperature variations. The TC scanning is performed after the simultaneous BOS-PIV imaging. As one field dimension is wider than the scanner stroke, the TC scanning is proceeded by two successive passes of medium height (170 mm). The total field is then reconstructed by the two passes data. A maximum stroke pass (285 mm) is also recorded to

check stitching issues. The probe position is kept 30 seconds for TC temperature stabilization, then the measurement sequence lasts 30 seconds. Around 6 hours are needed to complete the whole domain.

The best resolutions of the fields are 1.2, 1.3 and 2 mm for the PIV, BOS and TC scanning methods, respectively. The PIV value corresponds to a 24 pixels interrogation window with 75% overlap (200 µm/raw pixel). The BOS value corresponds to a 24 pixels interrogation window with 75% overlap (210 µm/raw pixel). Raw BOS and PIV images have undergone the same PIV algorithm by Davis® software. The 2 mm resolution corresponds to the tiniest difference between 2 vertical profiles swept by the TC near the hot wall. In the rest of the field the resolution is around 10 mm. Additionally, some supplementary measurements (flow rate and temperatures of the wall circulation, calorimetry balance) are achieved to determine the global heat transfer.

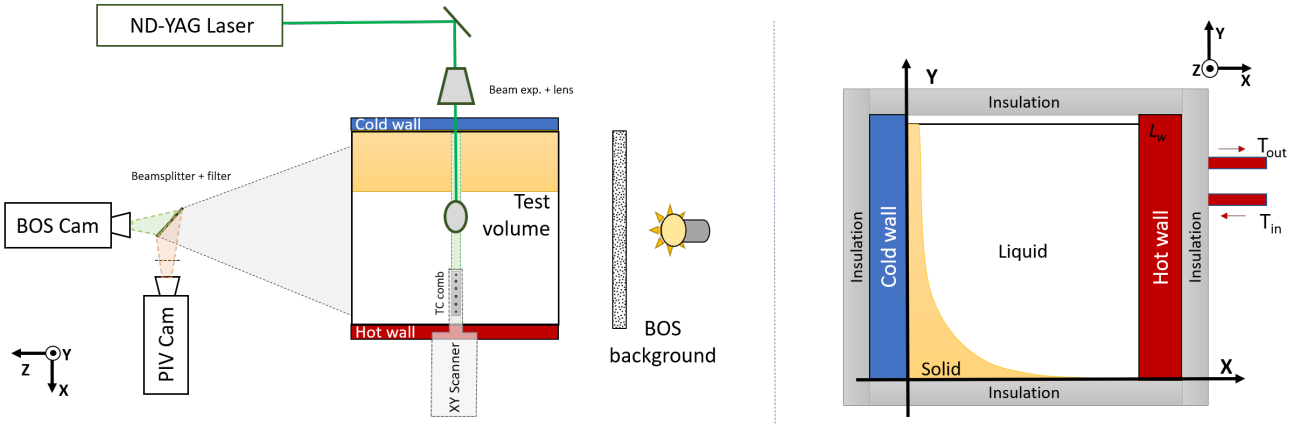


**Figure 1.** Top view sketch of the experimental apparatus (left); Front (cameras) view representation of the cubic test volume (right)

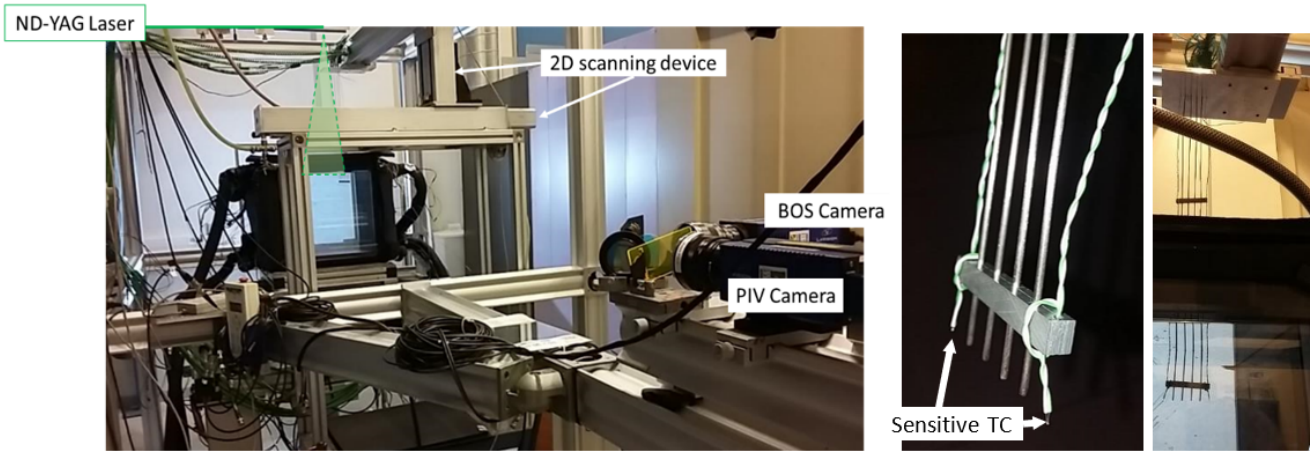


**Figure 2.** General view of the apparatus bench (left); Details of the 6 Thermocouples (TC) with sensitive high sensitivity/response TC at the extremities; the whole comb probe inserted in liquid PCM (right)

To study different thermal regimes, corresponding to a range of Rayleigh numbers, various temperatures $T_{hot}$ and $T_{cold}$ conditions are set. Measurements are performed at steady state (principal flow motion and solid/liquid interface) is steady. This stabilization was verified via the hot wall

power indicator, and the time before the beginning of the measurement varied from at least 3 hours (full liquid) to several days to ensure the stabilization of the solid-liquid interface.

## 3. Theoretical approach

### 3.1. BOS considerations

BOS technique is also known in the literature as Synthetic Schlieren and was initiated approximately at the same time by several authors (Dalziel et al., 2000; Meier, 2002; Raffel et al., 2000). It has been relatively well developed since 2000 (Raffel, 2015; Settles & Hargather, 2017). The principle is to capture the deformation of the light rays going through a refractive medium. The deformation displacement $\varepsilon_x$ of an image is proportional to the refractive index gradient $n$ of the medium. The equations vary from one source to another, but the relationship can be expressed as (Jensen et al., 2005)

$$\frac{\partial n}{\partial x} = Cst.\varepsilon_x. \tag{1}$$

As the observed volume is large, the assumption of parallel rays is most likely not valid over the whole domain. Moreover, placing the camera at a position following the moving interface is hard, while the Schlieren techniques are sensitive to optical alignments. The BOS visualization is considered only on the hot wall and in only 1D. It allows the characterization of the heat transfer at the wall for all interface configurations. Along the wall, 1Dimensional temperature field is considered as the vertical $y$ gradients are small compared to horizontal $x$ gradients. So the refractive index profiles along the $X$-axis can be determined thanks to Equation (1) on a line integral (Jensen et al., 2005). The mathematical development of the equations leads to an explicit formulation, with a Dirichlet boundary condition away from the wall

$$n(x) = n_0 + \int_{x_0}^{x_W} \frac{dn}{dx} dx \quad . \tag{2}$$

$$n(x) = n_0 + \int_{x_0}^{x_W} \text{Cst} \, .\varepsilon_x(x) \cdot dx \tag{3}$$

$$\text{Where Cst} = \frac{2n_0}{L_z(L_z + z_{cube-target})} \quad , \tag{4}$$

$$\begin{cases} n\left(x = x_0\right) = n_c \\ n(x + \Delta x) = n(x) + Cst.\varepsilon_x(x) \cdot \Delta x \quad , \end{cases} \tag{5}$$

Where $x_W$ and $x_0$ are the $X$-axis position of the wall and far from the wall, $n_0$ is the refractive index far from the wall and $\Delta x$ is the integration step along $x$ (BOS pixel), $L_z$ and $z_{cube-target}$ are

the test volume depth and the space between the cube and the target. Eventually, the temperature is recomputed thanks to the Gladstone-Dale formula. In particular, the constants $c_1$ and $c_2$ in Equation (6) are needed

$$T_{BOS_{Glad}}(x) = \frac{1}{c_1 \cdot n(x) + c_2} \quad , \tag{6}$$

$$\begin{cases} c_1 = \dfrac{\frac{1}{T_c} + \frac{1}{T_W}}{n_c + n_W} \\ c_2 = \dfrac{1}{T_W} - c_1 \cdot n_W \end{cases} . \tag{7}$$

The related constants are determined thanks to the thermocouples' measurements. The calculation of the coefficients for each integration line can be delicate and the issue is discussed in Section 4.1.

### 3.2. Thermal characterization with the Nusselt number

The Nusselt number provides a quantitative and qualitative assessment of the convective flows near the wall. The dimensionless thermal gradient can locally express the Nusselt number

$$Nu = \frac{dT^*}{dx^*}\Big)_{x^*=x_W^*} = \frac{L_y}{T_{W_{hot}} - T_{W_{cold}}} \cdot \frac{dT}{dx}\Big)_{x=x_W} \quad , \tag{8}$$

Where $T_{W_{hot}}$ and $T_{W_{cold}}$ are the hot and cold walls temperatures, $L_z$ is the test volume height. Depending on the considered technique, TC and BOS, local Nusselt numbers can be expressed as

$$Nu_{TC} = \frac{L_y}{T_{W_{hot}} - T_{W_{cold}}} \cdot \frac{dT}{dx}\Big)_{x=x_W} = \frac{L_y}{T_{W_{hot}} - T_{W_{cold}}} \cdot \frac{\Delta T_{TC}\,(x = x_W)}{\Delta x_{TC}} \quad , \tag{9}$$

$$\begin{cases} Nu_{BOS} = \dfrac{L_y}{T_{W_{hot}} - T_{W_{cold}}} \cdot \dfrac{dT}{dn} \cdot \dfrac{dn}{dx}\Big)_{x=x_W} = \dfrac{L_y}{T_{W_{hot}} - T_{W_{cold}}} \cdot \dfrac{dT}{dn} \cdot \text{Cst. } \varepsilon_x\,(x = x_W) \\ Nu_{BOS_{Glad}} = \dfrac{L_y}{T_{W_{hot}} - T_{W_{cold}}} \cdot \dfrac{\Delta T_{BOS_{Glad}}\,(x = x_W)}{\Delta x_{BOS_{Glad}}} \end{cases} . \tag{10}$$

The local Nusselt is point-dependent, therefore Y-dependent. In this study, the TC Nusselt is calculated from the two closest grid verticals separated by 2 mm. As some temperature fields present a discontinuity of gradient at the stitching region, the uncomplete but continuous gradient from one pass is also analyzed. For the BOS Nusselt number, 2 assumptions are given: with a constant temperature optical index dependence $\frac{dT}{dn}$, $Nu_{BOS}$ is directly proportional to the displacement at the wall; with the Gladstone-Dale assumption, by calculating $Nu_{BOS_{Glad}}$ from the temperature gradient obtained at the wall. In this study, for both methods, the maximum values (respectively

displacement and temperature gradient) within the adjacent pixels of the x-line of the wall are considered. The Global Nusselt number is the integral along the wall of each local $Nu$ (where $L_y$ is the wall height taken as the characteristic length)

$$\overline{Nu_{\text{method}}} = \int_{y=0}^{L_y} Nu_{\text{method}}\,(y) \cdot dy \quad . \tag{11}$$

These integrated Nusselt numbers can be compared to the global Nusselt characterized by calorimetry balance on the circulating water through the hot side wall. The hot wall Nusselt number $\overline{Nu_{hot}}$ is defined as the ratio of the effective power through the PCM $P_{hot}$ on the theoretical conductive power through the same PCM $P_{cd}$. The liquid value of the PCM conductivity is considered for the calculation. The hot power is corrected to consider the losses towards the cold wall outside the PCM (glass and steel supports) and towards the ambient air. The thermal conductance value between the hot and cold wall through the support $G_{th_{support}}$ is assessed from the materials' geometry and thermal conductivities; the thermal conductance between the hot wall and the ambiance $G_{th_{ext}}$ is set to correspond to a zero hot power when $T_{hot} = T_{cold\,wall}$. Therefore the $\overline{Nu_{hot}}$ yields

$$\overline{Nu_{hot}} = \frac{P_{hot}}{P_{cd}} \tag{12}$$

$$\text{Where} \begin{cases} P_{hot} = Q_{v_{hot}} \rho c_p \left(T_{in} - T_{out}\right) - G_{th_{support}} \left(T_{hot} - T_{coldwall}\right) - G_{th_{ext}} \left(T_{hot} - T_{ext}\right) \\ P_{cd} = G_{th_{PCM}} \left(T_{hot} - T_{coldwall}\right) = \dfrac{k^l_{PCM} L_y L_z}{L_x} \left(T_{hot} - T_{coldwall}\right) \end{cases} \tag{13}$$

Where $Q_{v_{hot}}$, $T_{in}$ and $T_{out}$ are the flowrate, the inlet and outlet temperatures of the circulation through the hot wall, respectively.

### 3.3. Fluid flow regime characterization with the Rayleigh number

The natural convection fluid flows are commonly characterized by the dimensionless Rayleigh number. It is expressed as the product of the Prandtl number and the Grashof number. The Grashof number involves a buoyancy term $\beta(T)(T_W - T_{cold})$ which raises an issue about the cold temperature, where $\beta$ is the coefficient of thermal expansion. As the dimensionless number characterize the fluid flow, the cold temperature considered is restricted by the melting temperature

$$T_{cold} = \max\left(T_{coldwall}, T_m\right) \quad . \tag{14}$$

This cold temperature $T_{cold}$ as well as the mean temperature $T$ are used in the expression of the following numbers

$$\begin{cases} Ra = \mathrm{Pr}\,.Gr \quad , \\ \mathrm{Pr}(T) = \dfrac{c_p(T)\nu(T)}{k^l_{PCM}(T)} \quad , \\ Gr\,(T_{hot}, T_{cold}, T) = g\dfrac{\beta(T)\,(T_{hot} - T_{cold})}{\mu(T)^2} * \rho(T)^2 L_y^3 \quad , \\ \text{Where } T = \dfrac{T_{hot} + T_{cold}}{2} \quad . \end{cases} \tag{15}$$

## 4. Results

### 4.1. Local measurements

The following results highlight the temperature and velocity fields for a particular temperature configuration with a solid-liquid interface : $T_{hot}$ = 34.8 °C; $T_{cold}$ = 11 °C. This configuration at an intermediate Rayleigh number $Ra$ and with a relatively high solid volume fraction was thus chosen for the interest of the study. In particular, the interface tracking in the left cold side as well as the characterization of heat transfer at the hot wall are shown. Heat transfer is characterized by the Nusselt number, reflecting the global or local thermal efficiency.
Figure 3 shows the BOS raw displacement along the $X$-axis after the correlation processing. From the raw images, each displacement profile was subtracted from its linear regression outside the boundary layer to reduce the optical disturbances. The corrected field after linear correction is also shown, as well as the refractive index field. The results for a field reconstruction close to the wall are to be compared with the TC scanning method in Figure 4.

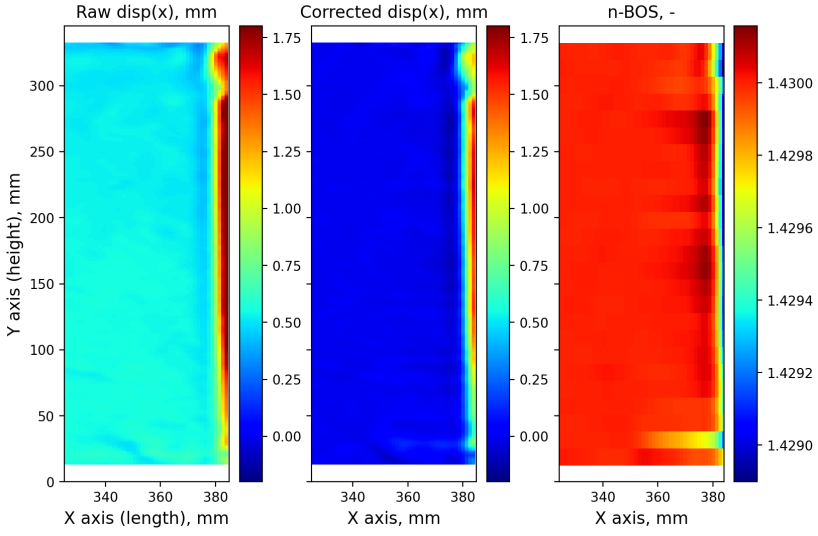


**Figure 3.** BOS 2D fields at hot wall: from raw displacement $\varepsilon_x$ to $n$-index ($T_{hot}$ = 34.8 °C, $T_{cold}$ = 11 °C)

Figures 5 and 6 show the velocity and temperature fields, for two different configurations for a Rayleigh number of $Ra = 3.1\ 10^8$ and $Ra = 9.0\ 10^8$, respectively. In these figures the measured variables only inside the relevant liquid domain is represented: a mask is applied for the velocity

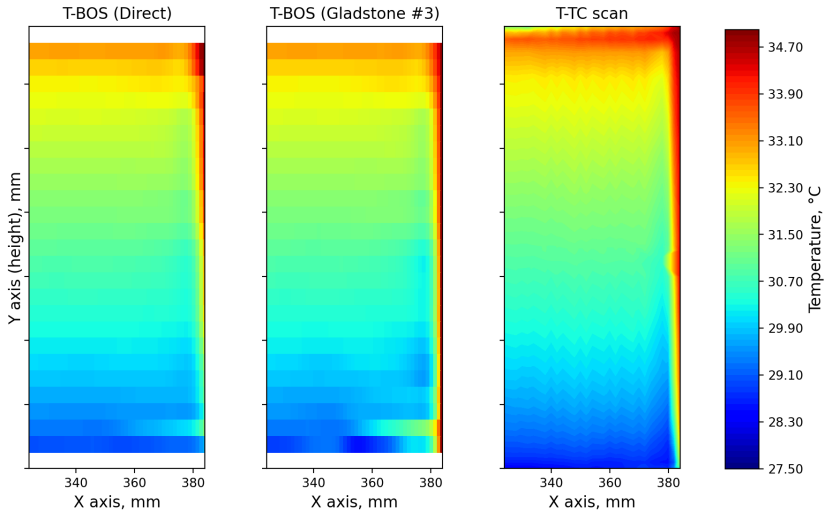


**Figure 4.** Temperature field comparison at hot wall: BOS 1D reconstruction Vs. TC scanning ($T_{hot}$ = 34.8 °C, $T_{cold}$ = 11 °C)

while the scanning TC can reveal only the intrinsic liquid temperature. In particular, the temperature range reduced to liquid limits permits to better visualize the thermal boundary layers at both walls, contrary to the cases with solid reconstruction.

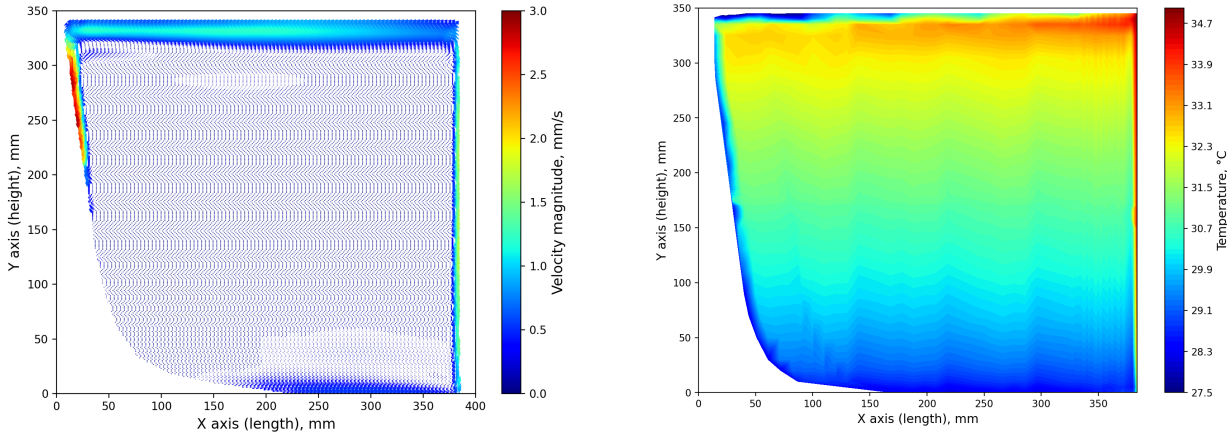


**Figure 5.** Velocity vector (PIV, left) and temperature fields (TC, right) fields for $Ra = 3.1\ 10^8$ ($T_{hot}$ = 34.8 °C, $T_{cold}$ = 11 °C)

As illustrated in Figures 5 and 6, the general flow presents two thin boundary layers (of a few millimeters) at both sides: on the right hot wall and the left solid/liquid interface. The flow is very slow in the central part but shows a temperature stratification, as visualized in both Figures 5 and 6. The zones of high gradients of temperature and velocity can be correlated, particularly at the end of the boundary layer on the hot wall (upper-right corner). The top part effects are more complicated to explain as these perturbations are partially due to natural convection and ambient air passing through the lid groove.

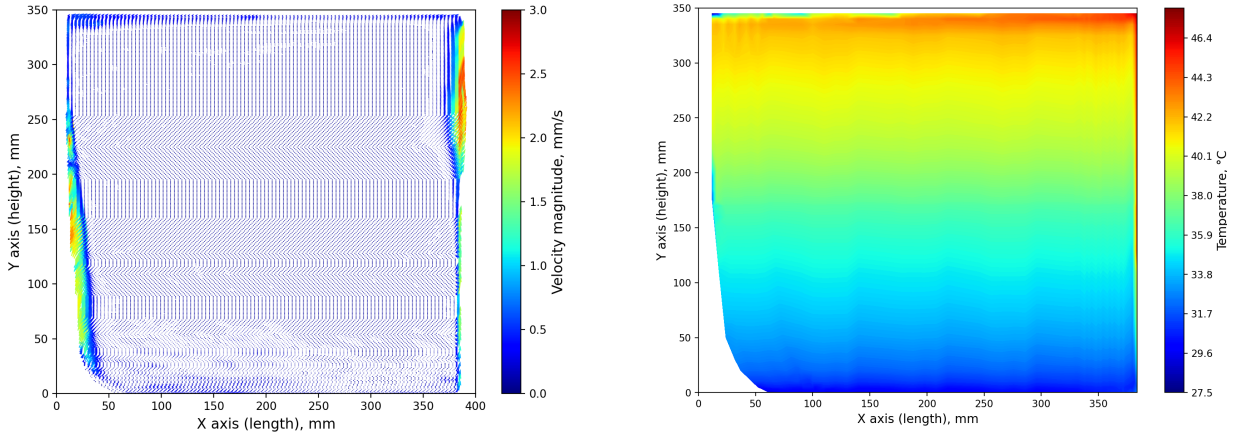


**Figure 6.** Velocity vector (PIV, left) and temperature fields (TC, right) fields for $Ra = 9.0\ 10^8$ ($T_{hot}$ = 47.5 °C, $T_{cold}$ = 8.9 °C)

The local Nusselt number representing the heat transfer along the hot wall is plotted for the different methods in Figure 7. Although the differences are significant, the trend is similar: as $Y$ increases, $Nu$ first grows and further decays. The Nusselt number first rises as the boundary layer expands (for increasing $Y$), like in a classical boundary layer. The difference with the classical boundary layer is that the ambient quasi-static fluid is not at constant temperature. Here, the ambient liquid is temperature-stratified. So, as the liquid rises in this layer, it encounters warmer and warmer static liquid, and the temperature gradient decreases even if the unsteady effects are more and more effective.

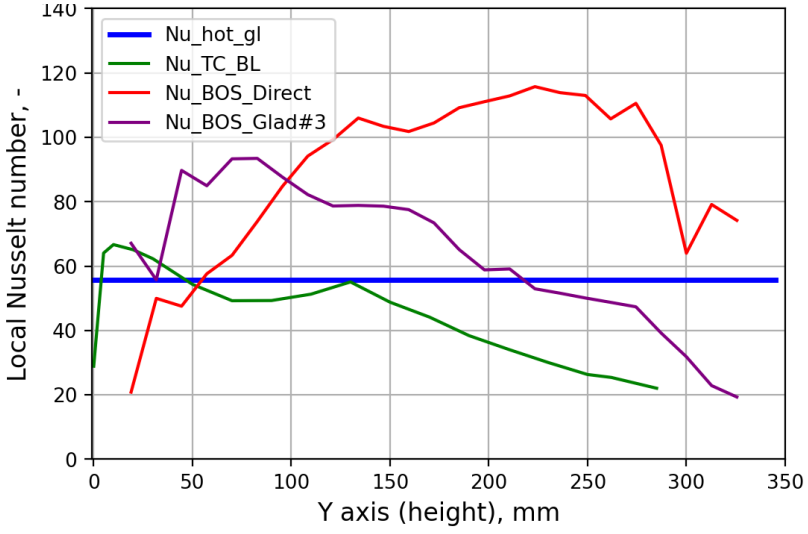


**Figure 7.** Comparison of local Nusselt number with TC and BOS methods ($T_{hot}$ = 34.8 °C, $T_{cold}$ = 11 °C)

### 4.2. Discussions on the measurement methods

The 2D field measurements present a few difficulties. First, the dimension of the boundary layers (a few millimeters thick) compared to the dimensions of the domain (0.4 m) renders the general accuracy complicated. To obtain the entire domain implies a relatively low resolution of the near-interface flow.
To improve the general resolution, it was not chosen to add more imaging system as already two cameras were used for this study. However, multiple points of view were firstly considered, undergoing a camera displacement. A four-quadrant camera motion was tested beforehand. Unfortunately, there were at least three issues to this solution. There were image fitting inaccuracies during the stitching process: a leap between images was remaining due to the even slight angle difference between quadrant camera location. Also, only averaged fields are relevant: all the unsteady variations due to natural convection close to the free surface or the boundary layer turbulence were impossible to be considered. Furthermore, repositioning the cameras to the quadrant change the optical views and the results are very sensible to the camera location and tilt angle, in particular the BOS via reference images. Also, the chosen methodology was already time and data consuming.

The other difficulties of the measurements in this study, especially due to disturbing phenomena close to the interfaces, are discussed in this section for each method.

The PIV inside a flow with interfaces is never trivial. Though they present a relatively different density (around 200 kg/m3 difference), the reflection on the walls is greatly avoided by the choice of the luminescent particles. The reflection/diffusion is then reasonably low for the two vertical and the free surfaces, but still intense at the bottom wall: blur on PIV camera due to sedimented particles and risk of damaging reflection on BOS camera. To protect both cameras an equivalent-2 mm-high line was hidden from the bottom field of view. The sedimentation causes another important issue because the motion of the liquid is slow and long before the regime stabilization. To guarantee a correct seeding, the liquid was mixed before every new configuration and measurement have occurred between 2 hours (mixing aftereffects) and 36 hours (sedimentation).
One can notice that the PIV field of the Figure 5 does not let appear the complete boundary layer at the lower part of the cold interface. This bias is due to the side effect on front and back glass walls. Indeed as the solid layer is locally thicker close to the front wall, the boundary layer is hidden, all the more so as the solid is thick. The high velocity flow is then only visible at the top of the cold wall, where the solid shell is thinner. The lower the hot wall temperature is set, the higher this phenomena occurs and the wider is the obstructed part of the field of view.

The thermocouples appear as a direct and robust measurement technique but present a few drawbacks. Even chosen as a compromise between the probe response time and the comb stiffness, the sunk scanning apparatus is invasive. The wide lengths of the scanned volume make it hard to be very accurate on the whole domain position and the dimensions of the thermocouples welding are

significant compared to the boundary layer. Furthermore, the positioning near the solid-liquid interface is not deterministic as the TC probe is soft and not contact-sensitive. Near a fixed wall, the position of the thermocouples can easily be programmed in the scan sequence while the positioning near the interface is visually set to be as close as possible without scratching during the probe motion. With the presence of the interface, the thermocouples do not always get into contact and the surrounding points are not as numerous so the boundary layer at the cold side is not resolved as accurately as it is close to the hot wall (Figure 6). The scanning is also very time-consuming, around 6 hours for each whole domain scan including 1 hour for the boundary layer pass.

The BOS method is completely non-invasive, but comprises two main difficulties: the optical system configuration choice involving the deviation of the rays in the whole domain and the reconstruction which is made hard because of the boundary conditions.
The former difficulty implies biases on the optical measurements. Firstly, the camera was positioned in the same plane as the hot wall, but it was changed after a few tests. Indeed the constant in the Equation (4) assessed from (Jensen et al., 2005; Lipkin & Kurtz, 1941) was too low for the method when the rays go through the whole boundary layer; the observed displacements were too large to be detected. The camera was then placed as centered on the whole domain, which represents a slight angle with the hot wall but a highly reduced effective crossing depth of the boundary layer. The technique cannot render the thermal gradients very close to the wall (about 2 mm) because of this bias. As the boundary layer grows with the height location, this could explain the very low gradient (and so local $Nu$) detected at the beginning of the profile (roughly below 100 mm). The BOS results with the first position are shown in the global results (Section 4.3) but appear in black and are discarded from the correlations.
The latter difficulty is the boundary conditions especially for Gladstone-Dale method: the constants $c_1$ and $c_2$ in Equation (7) can be discussed in regards with the instrumentation. From the variables of the Equation $T_c$, $T_W$, $n_c$ and $n_W$, the hot wall temperature $T_W$ is well known and the corresponding refractive index $n_W$ at the wall is considered constant at a value taken from literature (Lipkin & Kurtz, 1941). For the cold side, $n_c$ is calculated from the integral in Equation (6) for each $x$-line; $T_c$ can be differently fixed from TC measurements. The temperature relatively far from the wall can be considered as the interpolation of the $Y$-axis vertical profile or its median value. Hence, there are three possibilities for the calculation of the $c_1$ and $c_2$ Gladstone-Dale coefficients:

1. Same coefficients for all $x$-lines for one configuration (median $T_c$ and median $n_c$)
2. Different coefficients for each $x$-line, using median n (interpolated $T_c$ and median $n_c$)
3. Different coefficients for each $x$-line, using the calculated n (interpolated $T_c$ and median $n_c$)

For all assumptions, the temperature at the hot wall is then fixed, but only for assumption #3 the temperature is fixed at both sides as boundary conditions. Figure 8 shows the results from the three assumptions.

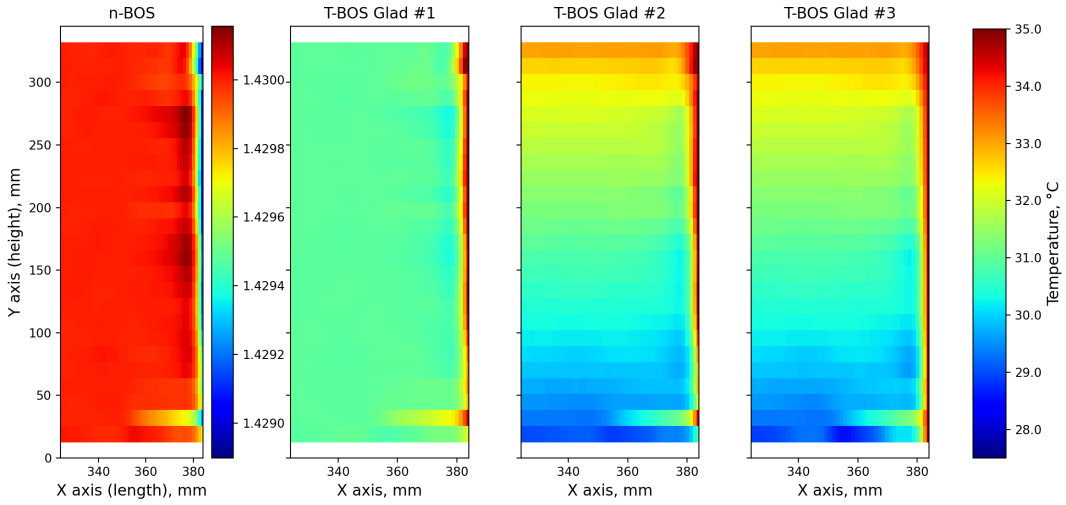


**Figure 8.** Influence of the Gladstone-Dale constants for the temperature reconstruction ($T_{hot}$ = 34.8 °C, $T_{cold}$ = 11 °C)

### 4.3. Global characterization

Different conditions with various wall temperature conditions have been tested. In total, measurements were achieved on 56 steady state configurations. In this section the global transfer as reflected by the global power and the Nusselt number values from Equation (11) are discussed. The external conditions have slightly changed from the first to the last data series. The global heat transfer with the ambient air has an influence on the global hot power, typically a few Watts. This global external conductance $G_{th_{ext}}$ from Equation (12) might lead to $\overline{Nu_{hot}}$ trend quite different especially at low Rayleigh number for which the convective power through PCM is low.

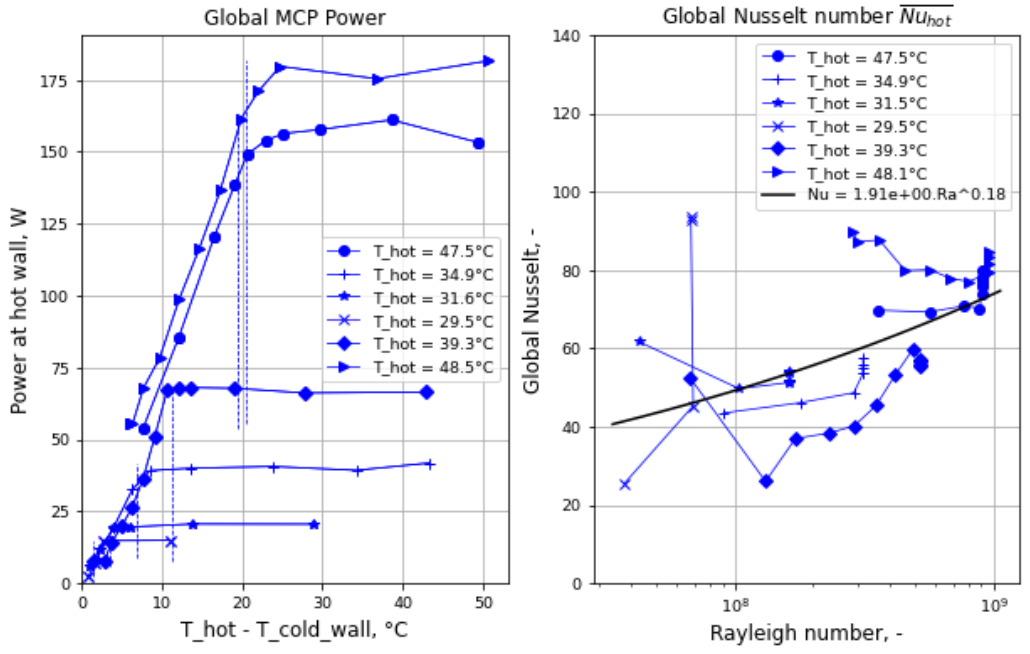


**Figure 9.** Global power at the hot wall $P_{hot}$ (left) and the resulting Nusselt number $\overline{Nu_{hot}}$ for each dataset (right)

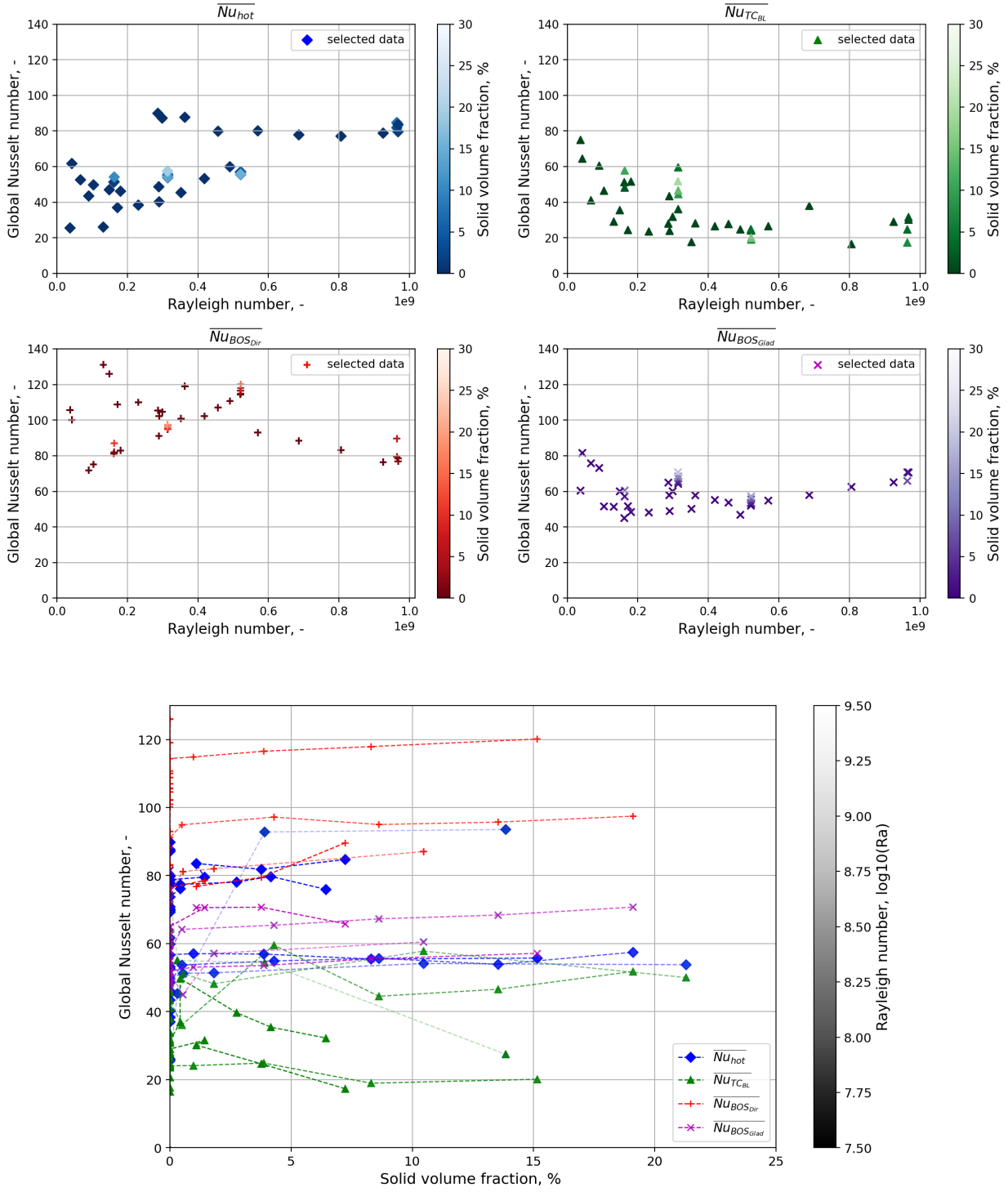


**Figure 10.** Representations of the global Nusselt numbers as function of the Rayleigh number (top) and the solid fraction (bottom)

It is important to note that the low Rayleigh number data should be considered with caution as the melting/solidification process close to the melting temperature is complex. It can present variations on the actual melting temperature with supercooling effect (typically 2 °C according to the RT28HC supplier (*Rubitherm GmbH*, n.d.)) as can be seen on the $T_{hot}$=29.5 °C batch on the Figure 9. Indeed, the melting temperature taken for the calculation is 28 °C but the global power continues to increase a lot below the theoretical melting temperature.

Figure 10 presents the summary of the global heat transfer characterization. The results appear as function of the Rayleigh number and the solid volume fraction. The solid fraction was calculated in the following results with the help of the TC scanning measurements: the interface was considered as the extreme positions of the thermocouples for each configuration scan. The general trend of the Nusselt number is not very clear according to the different methods. The primary dependence factor is the Rayleigh Number. Considering the hot power and the BOS Gladstone methods, the Nusselt number increases with the Rayleigh number. Considering the TC scanning and the BOS direct methods, the trend is more uncertain. The dependence of the solid fraction is lower but the effect is more clear: a slight increase in the Nusselt number when the solid fraction is increased.

## 5. Conclusions

We have described an experimental methodology adapted to Phase-Change Materials (PCM) to obtain the temperature, velocity, and heat transfer as reflected by the Nusselt number. The complex 2D two-phase flow represent a challenge for the experimental techniques. In particular, the characterization highlights some biases at the vicinity of interfaces (solid-liquid and walls). More accurate results could be obtained by focusing on a particular region of the domain. Our results form a data set of steady state configurations with an extended Rayleigh range. The next part of the study is to analyze some unsteady regimes with melting and solidifying flows. The formed database could be used to comprehend phenomena in large PCM containers and validate numerical models. In particular, the results on phase-change and turbulent regime represent a rare experimental matter that should help in this context.

## Acknowledgements

This work was conducted within the framework of ESP Carnot Institute (Energy and Propulsion Systems, COCHERMAT project). The Carnot institutes network is a French Research and Technology Organisation.

## Nomenclature

Variables

| | |
|---|---|
| $\beta$ | Thermal expansion coefficient [1/°C] |
| $c_p$ | Specific thermal capacity [J/(kg.°C)] |
| $\epsilon$ | BOS displacement [m] |
| $g$ | Gravitational acceleration [kg/(m.s$^2$)] |
| $Gr$ | Grashof number [-] |
| $G_{th}$ | Thermal conductance [W/°C] |
| $k$ | Thermal conductivity [W/(m.K)] |
| $L$ | PCM parallelepiped dimensions [m] |
| $n$ | Refractive index [-] |
| $\mu$ | Dynamic viscosity [Pa.s] |
| $\nu$ | Kinematic viscosity [m$^2$/s] |
| $Nu$ | Nusselt number [-] |
| $P$ | Power [W] |
| $Q_v$ | Volumic flow rate [m$^3$/s] |
| $Ra$ | Rayleigh number [-] |
| $\rho$ | Density [kg/m$^3$] |
| $T$ | Temperature [°C] |
| $x$ | Longitudinal coordinate [m] |
| $y$ | Vertical coordinate [m] |
| $z$ | Transversal/depth coordinate [m] |

Abbreviations and subcripts

| | |
|---|---|
| $BOS$ | Background Oriented Schlieren |
| $c$ | Cold side (wall or liquid) |
| $cd$ | Reference conduction |
| $ext$ | External (ambient) |
| $Glad$ | Gladstone-Dale ($n(T)$ law for BOS) |
| $hot$ | Hot wall |
| $l$ | Liquid |
| $m$ | Melting for temperature |
| $PCM$ | Phase Change Material |
| $PIV$ | Particle Image Veocimetry |
| $s$ | Solid |
| $TC$ | Thermocouple |
| $W$ | Wall |
| $*$ | Dimensionless |

**References**

Agyenim, F., Hewitt, N., Eames, P., & Smyth, M. (2010). A review of materials, heat transfer and phase change problem formulation for latent heat thermal energy storage systems (LHTESS). *Renewable and sustainable energy reviews*, *14*(2), 615–628. (Publisher: Elsevier)

Dalziel, S. B., Hughes, G. O., & Sutherland, B. R. (2000). Whole-field density measurements by 'synthetic schlieren'. *Experiments in fluids*, *28*(4), 322–335. (Publisher: Springer)

Dhaidan, N. S., & Khodadadi, J. M. (2015). Melting and convection of phase change materials in different shape containers: A review. *Renewable and Sustainable Energy Reviews*, *43*, 449–477. Retrieved 2021-12-14, from https://www.sciencedirect.com/science/article/pii/S1364032114009484 doi:

Faden, M., Linhardt, C., Höhlein, S., König-Haagen, A., & Brüggemann, D. (2019). Velocity field and phase boundary measurements during melting of n-octadecane in a cubical test cell. *International Journal of Heat and Mass Transfer*, *135*, 104–114. Retrieved 2021-05-06, from https://www.sciencedirect.com/science/article/pii/S0017931018331065 doi:

Jaguemont, J., Omar, N., Van den Bossche, P., & Mierlo, J. (2018). Phase-change materials (PCM) for automotive applications: A review. *Applied Thermal Engineering*, *132*, 308–320. Retrieved 2021-05-05, from https://www.sciencedirect.com/science/article/pii/S1359431117319762 doi:

Jensen, O. S., Kunsch, J. P., & Rösgen, T. (2005). Optical density and velocity measurements in cryogenic gas flows. *Experiments in fluids*, *39*(1), 48–55. (Publisher: Springer)

Lipkin, M., & Kurtz, S. (1941). Temperature coefficient of density and refractive index for hydrocarbon in liquid state. *Industrial & Engineering Chemistry Analytical Edition*, *13*(5), 291–295. (Publisher: ACS Publications)

Meier, G. E. A. (2002). Computerized background-oriented schlieren. *Experiments in fluids*, *33*(1), 181–187. (Publisher: Springer)

Raffel, M. (2015). Background-oriented schlieren (BOS) techniques. *Experiments in Fluids*, *56*(3), 60. Retrieved 2021-09-29, from https://doi.org/10.1007/s00348-015-1927-5 doi:

Raffel, M., Richard, H., & Meier, G. E. A. (2000). On the applicability of background oriented optical tomography for large scale aerodynamic investigations. *Experiments in Fluids*, *28*(5), 477–481. (Publisher: Springer)

Rostami, S., Afrand, M., Shahsavar, A., Sheikholeslami, M., Kalbasi, R., Aghakhani, S., … Oztop, H. F. (2020). A review of melting and freezing processes of PCM/nano-PCM and their

application in energy storage. *Energy*, *211*, 118698. Retrieved 2021-12-14, from https://www.sciencedirect.com/science/article/pii/S0360544220318065 doi:

*Rubitherm GmbH.* (n.d.). Retrieved 2022-04-08, from https://www.rubitherm.eu/en/index.php/productcategory/organische-pcm-rt

Sahoo, S. K., Das, M. K., & Rath, P. (2016). Application of TCE-PCM based heat sinks for cooling of electronic components: A review. *Renewable and Sustainable Energy Reviews*, *59*, 550–582. (Publisher: Elsevier)

Settles, G. S., & Hargather, M. J. (2017). A review of recent developments in schlieren and shadowgraph techniques. *Measurement Science and Technology*, *28*(4), 042001. Retrieved 2021-05-07, from https://doi.org/10.1088/1361-6501/aa5748 (Publisher: IOP Publishing) doi:

Souayfane, F., Fardoun, F., & Biwole, P.-H. (2016). Phase change materials (PCM) for cooling applications in buildings: A review. *Energy and Buildings*, *129*, 396–431. Retrieved 2021-12-14, from https://www.sciencedirect.com/science/article/pii/S0378778816302419 doi:

Sun, Z., Yang, P., Luo, K., & Wu, J. (2021). Experimental investigation on the melting characteristics of n-octadecane with electric field inside macrocapsule. *International Journal of Heat and Mass Transfer*, *173*, 121238. Retrieved 2021-05-06, from https://www.sciencedirect.com/science/article/pii/S0017931021003410 doi: